UNIVERSITY *of York*

This is a repository copy of *A new 12C + 12C nuclear reaction rate : Impact on stellar evolution*.

White Rose Research Online URL for this paper:
https://eprints.whiterose.ac.uk/187718/

Version: Published Version

Article:

Monpribat, E., Martinet, S., Courtin, S. et al. (10 more authors) (2022) A new 12C + 12C nuclear reaction rate : Impact on stellar evolution. Astronomy and Astrophysics. A47. ISSN 0004-6361

https://doi.org/10.1051/0004-6361/202141858

White Rose
university consortium
Universities of Leeds, Sheffield & York

eprints@whiterose.ac.uk
https://eprints.whiterose.ac.uk/

Astronomy & Astrophysics

A new ^{12}C + ^{12}C nuclear reaction rate: Impact on stellar evolution

E. Monpribat[1], S. Martinet[2], S. Courtin[1,3], M. Heine[1], S. Ekström[2], D. G. Jenkins[3,4], A. Choplin[5], P. Adsley[6,7],
D. Curien[1], M. Moukaddam[1], J. Nippert[1], S. Tsiatsiou[2], and G. Meynet[2]

[1] Université de Strasbourg, CNRS, IPHC UMR 7178, 67000 Strasbourg, France
   e-mail: `sandrine.courtin@iphc.cnrs.fr`
[2] Department of Astronomy, University of Geneva, Chemin Pegasi 51, 1290 Versoix, Switzerland
   e-mail: `sebastien.martinet@unige.ch`
[3] University of Strasbourg Institute of Advanced Studies (USIAS), Strasbourg, France
[4] Department of Physics, University of York, Heslington, York YO10 5DD, UK
[5] Institut d'Astronomie et d'Astrophysique, Université Libre de Bruxelles, CP 226, 1050 Brussels, Belgium
[6] Cyclotron Institute, Texas A&M University, College Station, TX 77843, USA
[7] Department of Physics & Astronomy, Texas A&M University, College Station, TX 77843, USA

ABSTRACT

Context. By changing the internal composition of stars, nuclear reactions play a key role in their evolution and spur their contribution to the chemical evolution of galaxies. The STELLA collaboration recently carried out new direct measurements of the ^{12}C + ^{12}C fusion cross section – one of the key reactions occurring in C-burning regions in massive stars. Using a coincidence technique, accurate measurements were obtained for many different energies, with the lowest energy explored according to the Gamow window for massive stars.
Aims. This work presents new ^{12}C + ^{12}C reaction rates in the form of numerical tables with associated uncertainty estimations, as well as analytical formulae that can be directly implemented into stellar evolution codes. We also describe the impact of these new rates on C-burning in stars.
Methods. We determined reaction rates for two cross section extrapolation models: one based on the fusion-hindrance phenomenon and the other on fusion-hindrance plus a resonance. We then compared our results to prior data. Using the GENEC stellar evolution code, we study how these new rates impact the C-burning phases in two sets of stellar models for stars with 12 $M_\odot$ and 25 $M_\odot$ initial masses, which were chosen to be highly representative of the diversity of massive stars.
Results. The effective temperatures of C-burning in both sets of stellar models are entirely covered by the sensitivity of the present experimental data and no extrapolation of the rates is required. Although the rates may differ by more than an order of magnitude for temperatures typical of C-burning, the impacts on the stellar structures during that phase remain modest. This is a consequence of the readjustment of the stellar structure to a change of nuclear reaction rate for reactions that are shown to be important for energy production. For the hindrance case, the C-burning phase is found to occur at central temperatures that are 10% higher than with the hindrance plus resonance rate. Its C-burning lifetime is reduced by a factor of two. This model, nevertheless, loses more entropy than the other one; thus, it enters into the degeneracy regime earlier, which will impact the last stages of the evolution at the pre-core collapse time. The hindrance model produces up to 60% more neon. The impact of the different rates on the *s*-process occurring during the C-burning phase is modest, affecting the final abundances of *s*-processed elements by at most 20% (cobalt).
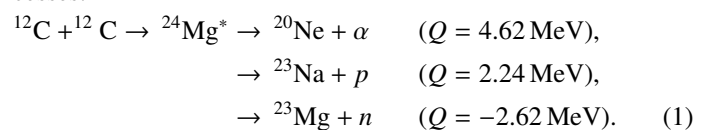
Key words. nuclear reactions, nucleosynthesis, abundances – stars: evolution – stars: massive

1. Introduction

The origin of the chemical elements in our Universe is one of the key questions driving contemporary subatomic physics. The Big Bang produced only hydrogen, helium, and trace amounts of lithium. The remaining 80 chemical elements in the Mendeleev Table are believed to have been forged through nuclear reactions in stars. In many cases, however, our understanding of the relevant nuclear reactions is incomplete; examples include the fusion processes taking place in a star such as the sun (Villante & Serenelli 2021), and the fusion of oxygen in massive stars (Holt et al. 2019). In this paper, we focus on carbon-fusion reactions that are the main energy source in the C-burning regions in a star. We start by recalling that the evolution of stars starts with H-burning, followed by He-burning, when carbon is synthesized, through the triple-alpha process. If the star is massive enough (with initial masses higher than $\sim 8\,M_\odot$), its temperature and density further increase and C-burning may start

(typically at temperatures above 0.6−0.8 GK), first at the centre of the star and then in a shell.

The carbon fusion reaction, ^{12}C + ^{12}C, leads to the formation of a ^{24}Mg* compound nucleus at an excitation energy around 15−17 MeV; subsequent particle emission leads to the residual nuclei, ^{20}Ne, ^{23}Na and ^{23}Mg, through the following set of processes:

$$
\begin{aligned}
^{12}\text{C} + ^{12}\text{C} \rightarrow {}^{24}\text{Mg}^* &\rightarrow {}^{20}\text{Ne} + \alpha \quad &(Q = 4.62\,\text{MeV}), \\
&\rightarrow {}^{23}\text{Na} + p \quad &(Q = 2.24\,\text{MeV}), \\
&\rightarrow {}^{23}\text{Mg} + n \quad &(Q = -2.62\,\text{MeV}). \quad (1)
\end{aligned}
$$

In an astrophysical context, the dominant exit channels are the alpha and proton channels, with the neutron emission channel being endothermic (Bucher et al. 2015). Together with these main fusion reactions, other reactions are important during the C-burning phase (see e.g. the book by Illiadis 2015). An important one is the reaction ^{23}Na$(p,\alpha)^{20}$Ne that converts nearly all

the ^{23}Na into ^{20}Ne. The elements most strongly produced by the C-burning phase are ^{20}Ne and ^{24}Mg.

The ^{12}C + ^{12}C fusion reaction has been extensively studied, for more than fifty years, using direct measurements (see e.g. Patterson et al. 1969; High & Čujec 1977; Becker et al. 1981; Aguilera et al. 2006; Barrón-Palos et al. 2006; Spillane et al. 2007; Bucher et al. 2015). Since the nuclei produced by the decay of ^{24}Mg*, ^{20}Ne, ^{23}Na, and ^{23}Mg nuclei are often produced in excited states, then going on to emit gamma rays, measurements of carbon fusion involves the detection of light particles or de-excitation gamma rays. The studies cited above were all based on the detection of either light charged particles or gamma rays. The results obtained were consistent for center of mass energies above and near the Coulomb barrier. However, for energies below the Coulomb barrier – the astrophysically interesting region where cross sections are small, down to the picobarn range – the associated astrophysical S-factors from different measurements often differ by several orders of magnitude. The uncertainties inherent in the published data make it difficult to perform model extrapolations down to the lowest energies (Li et al. 2020). Difficulties in extrapolating the S-factors mainly come from two different sources. First, unlike most heavy-ion fusion reactions, the ^{12}C + ^{12}C fusion cross section exhibits strongly oscillatory or resonant behavior on and below the Coulomb barrier (Almqvist et al. 1960). The narrow resonances in the cross section have traditionally been attributed to ^{24}Mg excited states with a special ^{12}C–^{12}C molecular configuration (Jenkins & Courtin 2015), while, more recently, it has been speculated that the origin of the oscillations is due to the low density of states in the ^{24}Mg compound nucleus (Jiang et al. 2013). The second difficulty comes from experimental backgrounds that are, from a practical point-of-view, unavoidable in such low cross section studies at the energies relevant to massive stars (see Sect. 2.2).

In the last decade, in order to reduce such backgrounds, Jiang et al. (2012) proposed a coincidence detection method, tailored to studies of ^{12}C + ^{12}C fusion; the first experimental results have been published in Jiang et al. (2018). More recently, this coincidence method has been used in two different direct measurements by Fruet et al. (2020) and Tan et al. (2020), and show consistent results. In this paper, we present new accurate reaction rates that can be incorporated into astrophysical models, based on direct measurements performed with a coincidence method, that have been obtained for centre of mass energy in the Gamow window for massive stars. The cross section data employed is derived from the direct measurement recently published by Fruet et al. (2020), which was obtained with the STELLA experiment (described more fully in Sect. 2.2).

New stellar models for representative masses in the massive star range were then computed with these new rates during the C-burning phase. Carbon-burning in stars has been studied for a long time (see e.g. Arnett & Truran 1969; Lamb et al. 1976; Weaver et al. 1978; Sparks & Endal 1980; Arnett & Thielemann 1985) but, interestingly, it still remains a topic of lively research today. For instance, Gasques et al. (2007), Pignatari et al. (2013) discussed the impact of the ^{12}C + ^{12}C rates on the s-process occurring in C-burning regions; Sukhbold & Adams (2020) studied the impact of the core C-burning phase on the final fate of red supergiants; Fields et al. (2018), in a very exhaustive study of the impact of nuclear uncertainties in models for pre-supernovae, identified, among the reactions having the largest impact on the pre-supernova structure, the reaction ^{12}C(^{12}C,p)^{23}Na; Chieffi et al. (2021) have investigated the impact of new rates for the carbon fusion reaction in stellar models.

As said above, in the present work, our aim is to explore the consequences of new rates for the carbon fusion reaction in stellar models. We also use simpler models, where we focus on the detailed abundances variations resulting from a very large nuclear reaction network (following more than 1400 isotopes). Compared to the recent work by Chieffi et al. (2021), here we use different experimental data for the nuclear reaction rates that, as we shall see, lead to very different consequences.

The paper begins by briefly presenting the nuclear experiment in Sect. 2. Section 3 discusses the results, and the tables and formulae that can be directly implemented in stellar evolution codes. Sections 4 and 5 discuss the impact of the new rates in, respectively, stellar models and in a simpler model ('one-layer model') with a very extended nuclear reaction network. Finally, a brief summary with some perspectives for future work are given in Sect. 6.

2. Direct measurement of fusion reactions of astrophysics interest: The STELLA experiment

2.1. Brief historical overview

Fusion is among the most studied processes in the collision of heavy ions at nuclear physics energies. The interactions between two colliding nuclei are, in general, described using the Coulomb and nuclear potentials, the sum of these forming the so-called Coulomb barrier (CB), which is the barrier nuclei need to overcome or tunnel through for fusion to occur. The fusion probability therefore depends on the characteristics of this barrier, such as its height and width. We recall that in a star, the energy of reactants is related to their thermal motion: the fusion of carbon occurs at center of mass energies in the range $E_{cm} \approx 1-3$ MeV. These energies are lower than the Coulomb barrier for ^{12}C + ^{12}C fusion reaction, $E_{CB} = 6.6$ MeV.

The first particle accelerators were developed in the 1930s allowing nuclear reactions to be studied for the first time. Such accelerators, however, could only accelerate light ions such as protons and it was not until the 1960s that accelerator technology had developed sufficiently that heavy-ion beams such as ^{12}C could be accelerated. An early focus with such accelerators was the study of heavy-ion fusion. The corresponding descriptions of the fusion cross sections were based on the transmission of the CB, and on the probability that a compound nucleus – the composite of the nucleons in the target and projectile – was formed during the collision. This compound nucleus, formed in a very hot state, would then emit particles (neutron, proton, alpha) subsequently leading to residual nuclei in an excited state that then emit gamma-rays.

In the 1980s, the exploration of fusion below the CB led to the measurement of cross sections which were, surprisingly, orders of magnitude larger than those predicted by simple tunneling through a 1D potential barrier. This was the discovery of heavy-ion fusion enhancement, which recognises that sub-barrier fusion critically depends on intrinsic degrees of freedom of the interacting nuclei: deformation, low-lying collective excitations, as well as the exchange of nucleons (Jacobs & Smilansky 1983; Dasgupta et al. 1998). Coupled-channel models, including couplings to all relevant degrees of freedom, subsequently proved extremely successful in describing fusion below the CB. In a coupled-channels calculation, the nuclear potential has an impact on the CB characteristics as well as on the coupling strengths.

In the early 2000s, advances in experimental techniques and detector technology allowed cross sections to be accurately

measured at deep sub-barrier energies, even down to cross sections in the nanobarn range (Jiang et al. 2002). A surprising effect found at such low energies is the phenomenon of fusion hindrance, that is, an unexpectedly steep fall-off in the fusion cross section systematically below the predictions of coupled-channels calculations using standard potentials. This was first explained either using the saturation property of nuclear matter (Mişicu & Esbensen 2006) or by adding a second potential barrier, which the system of colliding nuclei would have to overcome, after reaching a touching configuration, to finally fuse to form the compound nucleus (Ichikawa et al. 2007). More recently, another explanation was proposed, reminding us that nucleons are fermions and taking into account the Pauli repulsion effects in computing the fusion cross sections (Simenel et al. 2017). The argument that fusion hindrance might affect all nuclear fusion reactions at the lowest energies is still hotly debated. It is thus essential to understand the onset of this phenomenon, which usually occurs at excitation energies for the compound system of ∼10−20 MeV.

Hindrance has been observed in a large number of heavy-ion fusion reactions, most of them involving medium-mass to heavy nuclear systems. The occurrence of fusion hindrance has been much less explored in lighter systems, especially those of astrophysical interest. Measuring in those systems is therefore of great importance, since the relevant energy region for fusion hindrance to occur may correspond to the Gamow window, thus constraining S-factor extrapolations and models (Back et al. 2014).

2.2. The STELLA experiment

The direct measurement of cross sections down to the nanobarn level is very challenging from the point of view of background suppression, the necessity of handling intense beams, and the treatment of data associated with rare events. For example, in such measurements, the gamma-ray signal of interest often becomes significantly less than the environmental gamma-ray background, and minor isotopes, such as deuterium in water absorbed into the carbon target foils, produce dominant charged-particle backgrounds that can make discrimination of fusion charged particles highly challenging. Contemporary measurements therefore often employ coincident detection of light charged particles and gamma rays to significantly reduce the type of backgrounds discussed (Jiang et al. 2012).

An example of a system that employs the coincidence approach is the STELLA apparatus (Heine et al. 2018), which exploits several specific technical developments to maximise sensitivity and background rejection, tailored to the challenging application of measuring carbon-fusion at very low cross sections. STELLA combines double-sided silicon strip detectors for charged-particle detection with an array of LaBr$_3$(Ce) gamma-ray detectors (Roberts et al. 2014) that offer excellent timing resolution (Heine et al. 2018). Data are collected using a triggerless data acquisition system. To support the high beam currents required for such studies, a rotating target mechanism is employed to efficiently dissipate heat in the thin self-supporting target foils, allowing for beam intensities of several microamps to be safely handled. The stability of the detection system is monitored offline during data-taking periods of months. Accuracy at the lowest counting rates (Feldman & Cousins 1998) is achieved by comparing sparse count measurements with an intrinsic background estimation (Fruet et al. 2020).

3. Results

3.1. Cross sections

The sub-barrier ^{12}C + ^{12}C fusion excitation function exhibits a series of resonances (Aguilera et al. 2006). The present deep sub-barrier data suggest the existence of an intermediate energy region with hindrance trend (see Fruet et al. 2020) and an onset of dominant resonance structures towards even lower energies. Therefore, two scenarios have been explored. The first one considers that the cross section follows an empirical model of fusion hindrance (Hin model). The second one is based on the hindrance model, on top of which a resonance proposed by Spillane et al. (2007) has been added (HinRes model). The Hin-Res model provides a better fit to the measured cross section data, but the presence of the resonance suggested by the data point at the lowest measured energy may need confirmation from further experiments. The procedure is described in the following paragraphs.

An excitation function for the Hin model has been obtained by fitting data measured by the STELLA Collaboration – Fruet et al. (2020) – with a dependency suggested by Jiang et al. (2007):

$$\sigma(E)_{\mathrm{hin}} = \sigma_{\mathrm{s}} \frac{E_{\mathrm{s}}}{E} \exp\left(A_0(E - E_{\mathrm{s}}) - \frac{2B_0}{\sqrt{E_{\mathrm{s}}}} \left(\sqrt{\frac{E_{\mathrm{s}}}{E}} - 1 \right) \right), \qquad (2)$$

where the parameters E_{s} and σ_{s} are the center of mass energy and the total cross section, respectively, for which the S-Factor $S(E)$ is maximum, and A_0 and B_0 are fitting parameters. All parameters are free during the adjustment of $\sigma(E)_{\mathrm{hin}}$ to STELLA data. The formula describing the total cross section was scaled by branching ratios from previous experimental data (Pignatari et al. 2013), corresponding to 35% for the proton exit channel and 65% for the alpha exit channel.

In the second scenario (HinRes), a resonance is added on top of the Hin model at the lowest energy; the contribution from an isolated narrow resonance described by the one-level Breit-Wigner cross section formula is:

$$\sigma_{\mathrm{BW}}(E) = \frac{\lambda^2}{4\pi} \frac{(2J + 1)(1 + \delta_{01})}{(2j_0 + 1)(2j_1 + 1)} \frac{\Gamma_a \Gamma_b}{(E_{\mathrm{R}} - E)^2 + \Gamma_{\mathrm{R}}^2/4}, \qquad (3)$$

where j_0 and j_1 are the spins of target and projectile respectively, J and E_{R} are the spin and the center of mass energy of the resonance, Γ_a and Γ_b are the resonance partial widths of entrance and exit channel, Γ_{R} is the total resonance width, and δ_{01} is the Kronecker delta. Values of the resonance parameters are kept fixed throughout the rest of this work. The cross section considered for this second scenario is the sum of Hin model cross section and the Breit-Wigner cross section.

The parameters were adjusted in both exit channels simultaneously in the range covering the expected hindrance maximum in the fitting procedure. Values of these parameters are given in Table 1. They are consistent with those predicted by Jiang et al. (2007), with a cross section maximum at energy $E_{\mathrm{s}} = 3.69$ MeV.

The cross sections and interpolations are shown in Fig. 1: in red for the Hin model and in green for the HinRes model. The cross sections predicted by Caughlan & Fowler (1988) (CF88 model) are also presented in blue. The cross sections have been extrapolated here down to an energy of $E_{\mathrm{rel}} = 1.2$ MeV.

We observe that at energies near the Coulomb barrier (i.e. $E_{\mathrm{CB}} = 6.6$ MeV), the models overlap, but diverge towards the lower energies, where the Hin model is slightly below that of the CF88 model. The resonance predicted by Spillane et al. (2007)

Table 1. Parameters of cross sections for $^{12}C + {^{12}C}$ fusion reaction using different models from data interpolation.

Model	σ_s $(10^{-2}$ mb)	E_s (MeV)	A_0 (MeV^{-1})	B_0 $(10^1$ MeV$^{1/2}$)	$((\omega\gamma)_R)_\alpha$ (MeV)	$((\omega\gamma)_R)_p$ (MeV)	Γ_R (keV)	E_R (MeV)
Hin	2.20 ± 0.14	3.69 ± 0.01	-1.16 ± 0.03	5.13 ± 0.02	$\varnothing$	$\varnothing$	$\varnothing$	$\varnothing$
HinRes	2.20 ± 0.14	3.69 ± 0.01	-1.11 ± 0.03	5.09 ± 0.02	0.11 ± 0.03	0.02 ± 0.03	12	2.138 ± 0.006
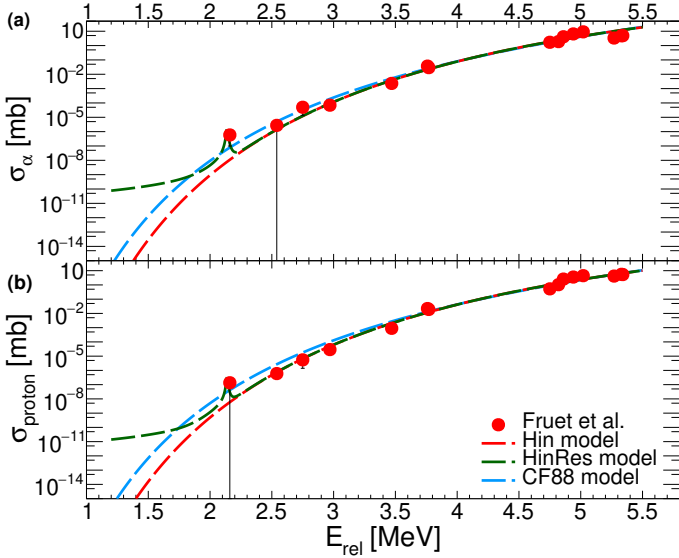
Fig. 1. Cross sections for alpha (*a*) and proton (*b*) channels, obtained with STELLA (red points). Adjustments made for the Hin model (red curve) and HinRes model (green curve) are compared with the cross section from the CF88 model (blue curve). Data points at the lowest energy for protons and the second lowest for the α channel are upper limits (vertical black lines).

shows a good compatibility with the STELLA measurements at the resonance energy. For energies below $E_{rel} = 2$ MeV, we note that while the cross section extrapolations from the Hin model and the CF88 model follow the same trend, the cross section from the HinRes model follows the tail of the resonance.

3.2. Reaction rates

In a general way, the stellar reaction rate $(N_A \langle \sigma v \rangle)$ can be expressed as (Rolfs & Rodney 1988):

$$(N_A \langle \sigma v \rangle) = \left(\frac{8}{\pi\mu}\right)^{1/2} \frac{N_A}{(kT)^{3/2}} \int_0^\infty \sigma(E) E \exp\left(-\frac{E}{kT}\right) dE, \qquad (4)$$

where N_A is Avogadro's number, μ is the reduced mass of the system, k is the Boltzmann constant, T is the temperature at which the reaction occurs, $\sigma(E)$ is the reaction cross section, and E is the center of mass energy. The total cross section $\sigma(E)$ is obtained by summing the cross section from all exit channels.

In the HinRes scenario, the reaction rate is determined by adding a rate specific to a single narrow resonance to the one described in Eq. (4). Illiadis (2015) define it as:

$$(N_A \langle \sigma v \rangle)_{res_i} = \frac{1.5399 \times 10^{11}}{\left(\frac{M_0 M_1}{M_0 + M_1} T_9\right)^{3/2}} \sum_i ((\omega\gamma)_R)_i \exp\left(-11.605 \frac{(E_R)_i}{T_9}\right), \qquad (5)$$

where i labels each resonance, $((\omega\gamma)_R)_i$ and E_R are the resonance strength and energy, M_i is the reactant atomic mass, and T_9 is the temperature (in GK) at which the reaction occurs.

The reaction rates obtained are shown in Fig. 2, in red for the Hin model and green for the HinRes model. The stellar reaction rate predicted in Caughlan & Fowler (1988) $(N_A \langle \sigma v \rangle)_{CF88}$ (CF88 rate) is also presented in blue. The orange hatched areas show the STELLA sensitivity, that is the temperature region where no extrapolation of the cross sections measured by STELLA is required. The shaded areas around each curve show the total uncertainties in the reaction rates, determined through error propagation of experimental uncertainties in the STELLA cross sections. The central temperature during C-burning phase (which begins here when 1% of the carbon abundance in the core is consumed, and ends when this same abundance is less than 10^{-5}), determined with data from Fig. 3, are also shown, for both stellar models studied in Sect. 4, and for both nuclear fusion scenarios considered in this work.

In the Hin scenario, the results obtained show that the reaction rate from STELLA data and the hindrance model is lower than that predicted by the CF88 model at low temperatures, but is similar to it at high temperatures, which is consistent with the predictions of Jiang et al. (2007).

In the HinRes scenario, the reaction rate is essentially the same as the one without a resonance, and it persists lower that the one predicted in CF88. However, we can see that the resonance exhibits two main effects. It slightly increases the reaction rate at low energies, and, in an intermediate region between $T = 0.5$ and 1.5 GK, it significantly increases the reaction rate to a level comparable with the CF88 rate.

The lowest centre-of-mass energy reached in the STELLA experiment is $E = 2.03$ MeV (see supplements in Fruet et al. 2020), corresponding to the Gamow energy at $T = 0.77$ GK. In the present case, the Gamow window can be very well approximated by a Gaussian function with the left side sigma-interval, that is a 68.27% probability coverage, translating into a lower temperature $T = 0.60$ GK. We associate this value to the sensitivity limit of the present experimental fusion-measurement data for detecting either a Hin or a HinRes trend, within the commonly used one-sigma significance-level.

In the temperature range of $T = 0.6 - 4.3$ GK, the relative uncertainty of the fits for the Hin model is below 15% and only becomes 31% towards lower temperatures in the case of the HinRes trend, due to the large uncertainties of the resonance parameters.

4. Stellar models

In this section, we explore the impact of the results obtained in Sect. 3.2 on stellar evolution models. Using GENEC (Eggenberger et al. 2008), we computed three sets of models using, respectively, $^{12}C + {^{12}C}$ reaction rates from Caughlan & Fowler (1988, hereafter CF88), the Hin model, and the HinRes model developed in the present work. For each of
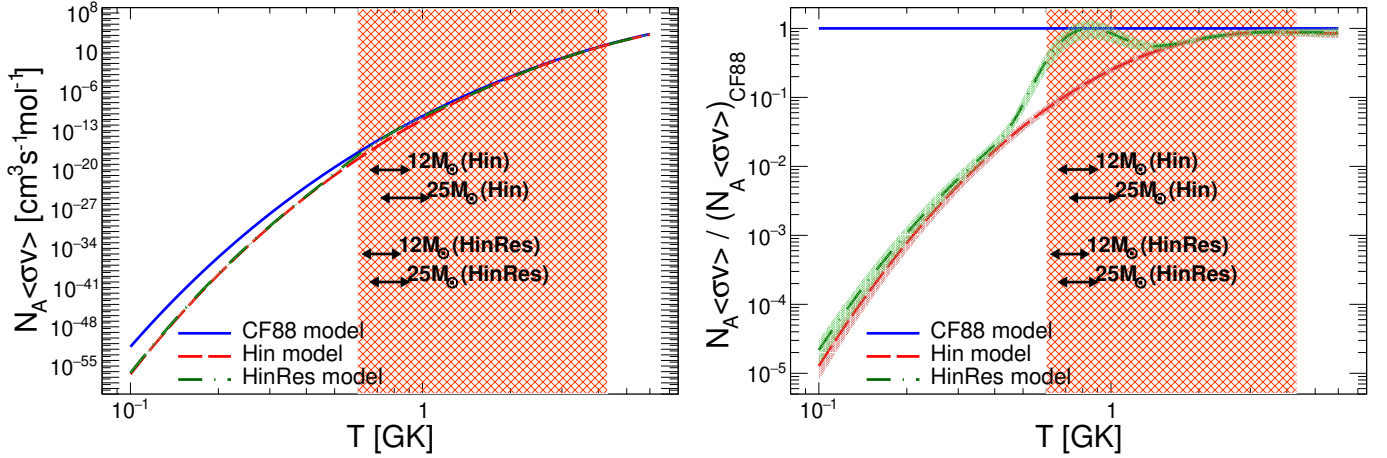
Fig. 2. Reaction rates (*left*) and normalized reaction rates to $N_A\langle\sigma v\rangle_{CF88}$ (*right*), without (Hin; red curve) and with (HinRes; green curve) the added resonance. The reaction rate from the CF88 model is also presented (blue curve). The shaded areas around the curves are the uncertainties (see text). Orange hatched areas show the temperature region explored by the STELLA experiment. The black arrows show the regions where carbon fusion occurs, for two stellar models (12 and 25 $M_\odot$), for both the Hin and HinRes models (see Sect. 4 and Fig. 3).
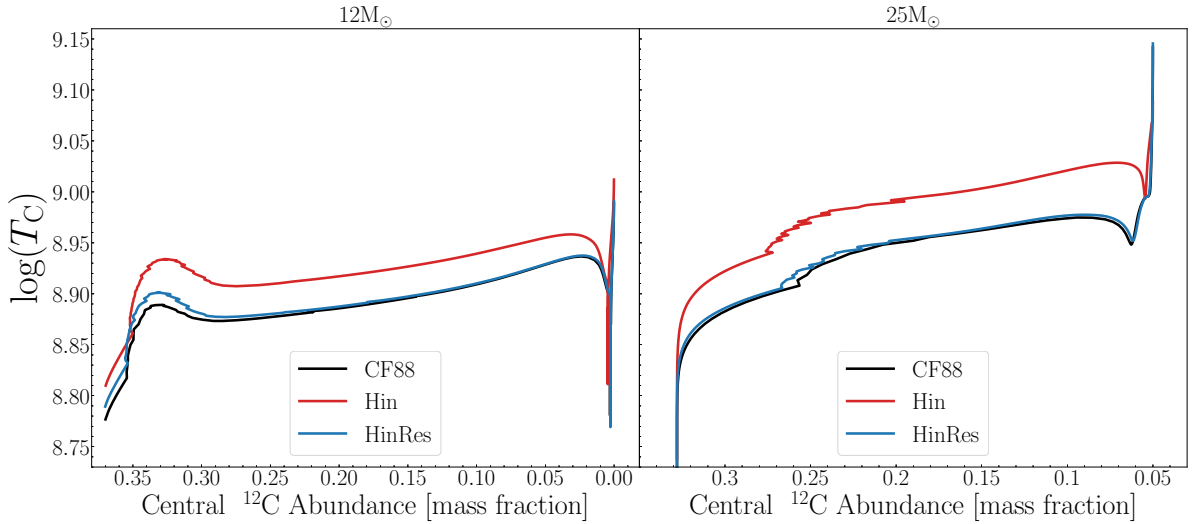
Fig. 3. Central temperature evolution during the C-burning phase for 12 $M_\odot$ and 25 $M_\odot$ models with different ^{12}C + ^{12}C reaction rates. The evolution is given as a function of the mass fraction of carbon at the centre that decreases as a function of time.

these sets, we computed the evolution of a non-rotating 12 $M_\odot$ and 25 $M_\odot$ star at $Z = 0.014$ (solar-like) until the end of the core C-burning phase. For a given initial mass, all the models share the same evolution up until the end of He-burning. Other than the ^{12}C + ^{12}C reaction rates, the physics inputs used for these models are the same as those described in Ekström et al. (2012).

Figure 3 shows the evolution of central temperature during the C-burning phase for different ^{12}C + ^{12}C reaction rates. The models with a lower rate (Hin model) burn carbon at a slightly higher central temperature (the relative increase is about 10%). The fact that lowering a rate produces an increase of temperature is due to the following well known fact: a lower rate implies less energy released per unit time. On the other hand, the energy lost per unit time at the surface of the star is not mainly determined by the nuclear reaction but by the hydrostatic and radiative equilibrium. To compensate for these losses at the surface when the nuclear energy production is less efficient, the core contracts in order to achieve a new hydrostatic or radiative equilibrium. The contraction increases the central temperature and thus the nuclear reaction rates and, hence, the energy released per unit

time. We note that since the dependence of the nuclear reactions on temperature is very high for the carbon fusion reaction (typically the rates depend on T^{27}), a small increase is sufficient to restore the equilibrium.

The situation with the HinRes model is not much different from the case with CF88 rate. The resonance decreases the maximum temperature where the hindrance effect would be non-negligible and, as seen in Fig. 2, the rate at the peak of the resonance is on the order of the CF88 rates. We see here that in stellar conditions during C-burning, the central temperature is in a range where the presence of the resonance is effective, dampening the hindrance impact; hence, the hotter medium for the 25 $M_\odot$ model shows even fewer differences than the 12 $M_\odot$ one between the CF88 rates and the HinRes rates.

The evolution of central conditions is shown in the temperature over density diagram in the left panel of Fig. 4. The core C-burning phase occurs when the bump occurs along the tracks that is around 0.8 GK (Log T = 8.9). The bump in the 12 $M_\odot$ track is particularly well developed. This results from the fact that carbon-ignition occurs in a medium mildly degenerated (the
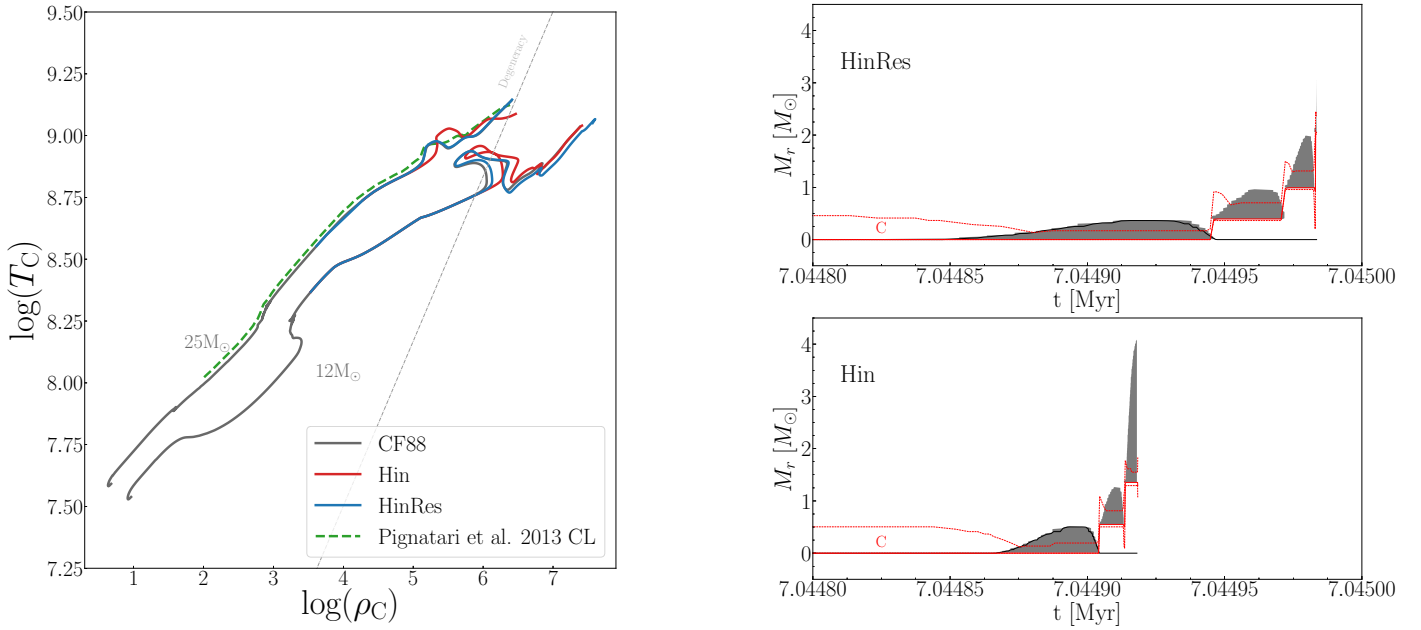
Fig. 4. Evolution of central temperature as a function of central density for $12\,M_\odot$ and $25\,M_\odot$ models with different $^{12}C + ^{12}C$ reaction rates (*left panel*). Kippenhahn diagrams for the centre of $25\,M_\odot$ models during the end of C-burning phase with Hin and HinRes $^{12}C + ^{12}C$ reaction rates (*right panel*). The grey shaded area shows the convective zones. The red dashed line show the limits of the C-burning zones (defined where $\epsilon_C \geq 10^2\,\mathrm{erg\,g^{-1}\,s^{-1}}$).

grey straight lines give the positions in the plane where the perfect gas pressure is equal to the non-relativistic electronic degenerate pressure). As seen in Fig. 4, the Hin model show bumps that are shifted to slightly higher densities and temperatures with respect to the other models. This results from the fact that these models have more compact cores during the C-burning phase. For comparison, the $25\,M_\odot$ model using the 'lower limit' from Pignatari et al. (2013) is superimposed in green. This model uses rates close to our HinRes one and consistently follow a very similar path as our HinRes model.

The right panel of Fig. 4 shows the Kippenhahn diagrams during the end of C-burning for the $25\,M_\odot$ models. It shows that the C-burning region (red, dashed lines) evolves in the same way for the different reaction rates. However, the convective zones developing in the inner regions of the star at the end of C-burning, when Ne-burning sets up, are quite different for the Hin model. Indeed, the convective zone, fueled by shell C-burning, extends much further away in the Hin model (see lower panel) compared to the HinRes model (upper panel). This effect is not present in the $12\,M_\odot$ models, hence, their Kippenhahn diagrams are not shown here. The largest convective zones in the Hin $25\,M_\odot$ model are likely due to the fact that, as already mentioned above, C-burning occurs at higher temperatures due to the lower nuclear energy generation rate in this temperature range. A stronger temperature gradient builds up that favors the occurrence of a larger convective zone. The situation in the $12\,M_\odot$ model is different due to the fact that we are in a medium that is more affected by degeneracy.

Figure 5 compares the abundance profiles of the $12\,M_\odot$ and $25\,M_\odot$ models for different $^{12}C + ^{12}C$ reaction rates obtained at the end of the core C-burning phase (i.e. the last model before the central carbon abundance is lower than 10^{-5}). In the left panel, only the central $1.75\,M_\odot$ are shown for the $12\,M_\odot$ model, above this regions, the models present no differences between them. In the right panel, the whole structure of the $25\,M_\odot$ is shown. We see that the chemical structure at the end of the C-burning is not

much affected by the changes of the rates in the $12\,M_\odot$ model. We note, however, some differences between 1.3 and $1.7\,M_\odot$. The mass coordinate at which the carbon abundance changes abruptly (around $1.44\,M_\odot$) shifts outwards by about $0.1\,M_\odot$ passing from the Hin model to the CF88 model and again passing from CF88 to the HinRes model. This abrupt change in abundance is due to presence of a convective C-burning shell. These differences, although non-negligible, are not very significant when considering other uncertainties linked to the treatment of convection in stellar models (see e.g. Gabriel et al. 2014; Kaiser et al. 2020).

We also observe a difference in the positions of the sharp change of the carbon abundance in the $25\,M_\odot$ models depending on the rates used. For the Hin model, the step occurs at about $4\,M_\odot$, while for the CF88 and HinRes model, the step occurs around $2\,M_\odot$. Here, we can see that in Hin model, the step is shifted outwards with respect to the other two models, while, as shown above, it was shifted inwards in the $12\,M_\odot$. This difference between the 12 and the $25\,M_\odot$ models comes from the extension of the convective C-burning shell, which is slightly more extended for the CF88/HinRes models in the $12\,M_\odot$ than the Hin one, while it is largely extended in the $25\,M_\odot$ Hin model compared to the CF88/HinRes ones. Indeed, the size of the convective regions strongly impact the chemical structure by imposing flat chemical gradients in them. The shift outwards of the sharp carbon abundance step in the $25\,M_\odot$ Hin model is linked to the extension of the last intermediate convective zone that we can see in the bottom panel of Fig. 4. This convective shell indeed extends up to around $4\,M_\odot$, while its maximum outwards extension in the HinRes model is limited to around $2\,M_\odot$ (see the upper panel of Fig. 4).

These two different behaviours for the 12 and $25\,M_\odot$ models illustrate the complex non-linear behaviour of the stars whose evolution results from many tightly intertwined processes.

We may wonder whether these differences in the chemical structure have an impact on the total quantity of an element in
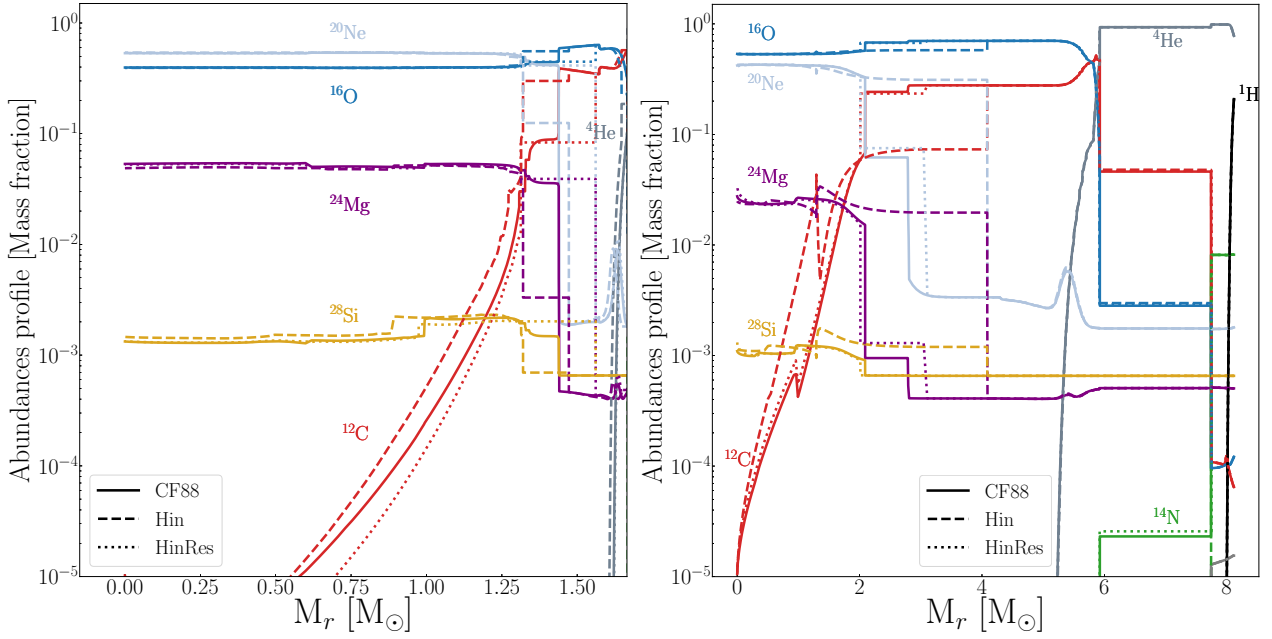
Fig. 5. Core abundances profile at the end of central C-burning for 12 $M_\odot$ models with different ^{12}C + ^{12}C reaction rates (*left panel*). Abundances profile at the end of C-burning for 25 $M_\odot$ models with different ^{12}C + ^{12}C reaction rates (*right panel*).
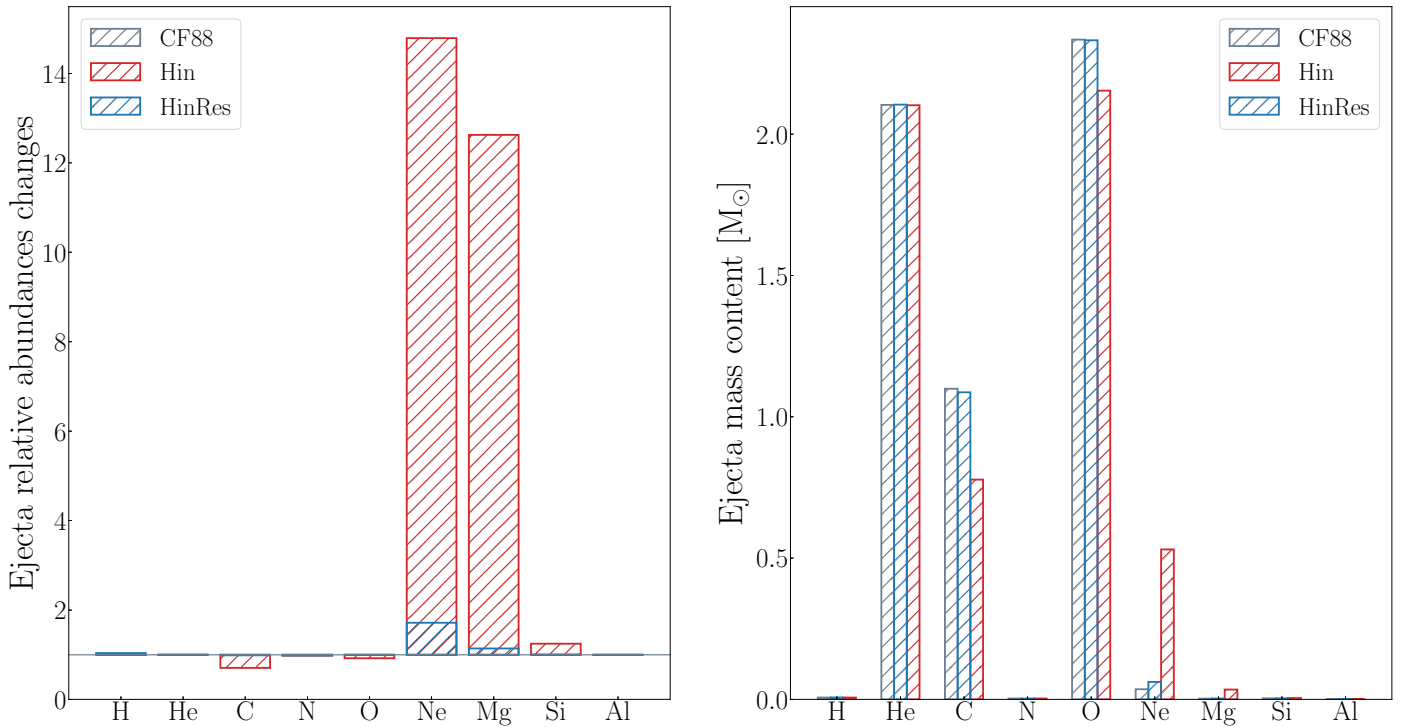
Fig. 6. Abundances relative to CF88 models in the supernova ejecta of the 25 $M_\odot$ models for different ^{12}C + ^{12}C reaction rates (based on the structure obtained at the end of the C-burning phase) (*left*). The same abundances but for the total mass content in the ejecta (*right*).

the outer envelope of the star. At the end of the C-burning phase, the envelope has nearly reached its final chemical composition because the subsequent nuclear phases will occur in regions well below this envelope and the time that remains before the explosion is so short that any changes in the envelope have no time to be become significant. Moreover, the explosive nucleosynthesis will affect mainly those layers near the core and the abundances of elements around the iron peak. Thus, it makes sense to look at the abundances of some light elements in the outer layers, that

is, in the layers that can be possibly ejected at the time of the supernova and see whether changes are seen depending on the rates used.

In Fig. 6, we compare the chemical composition in the supernova-ejecta of our different models. We use the structure of the envelope obtained at the end of C-burning as a proxy for its structure at the pre-supernova stage. The CO-core masses of those models (5.9 $M_\odot$) being almost equal (less than 0.1% of difference), we deduced from the relation between CO-core and the

Table 2. Central C-burning lifetime for different ^{12}C + ^{12}C reaction rates.

^{12}C + ^{12}C	CF88	Hin	HinRes
12 $M_\odot$	7604 yr	3856 yr	6698 yr
25 $M_\odot$	820 yr	403 yr	717 yr

remnant mass given in Maeder (1992) a common remnant mass of 2.4 $M_\odot$. We compute the quantities of various isotopes present in all the layers above the remnant mass to obtain the numbers shown in Fig. 6. Looking at the left panel, we see that the most affected elements are those which are the main products of C-burning, there are neon and magnesium. Their abundances are boosted in the Hin and HinRes models. This is likely because the duration of the C-burning phase is slightly/significantly reduced in the HinRes/Hin models (see below), offering less time for these two elements to be destroyed by α captures (i.e. by the reactions ^{20}Ne(α,γ)^{24}Mg(α,p)^{27}Al).

Table 2 shows the central C-burning lifetimes, computed when 1% of central ^{12}C abundance has been burnt up to the central ^{12}C abundance reaching value lower than 10^{-5}. The C-burning lifetimes are very similar between models with the CF88 rates and models using the HinRes reaction rates. Using solely the Hin reaction rates halves the lifetimes in comparison to the other models, due to the higher central temperature regime. Interestingly Chieffi et al. (2021), using rates that are much higher than those of Caughlan & Fowler (1988) in the 0.1−1 GK range, find that C-burning occurs at lower densities (see Fig. 3 in Chieffi et al. 2021). Indeed, since the nuclear rates are higher, a lower density is needed to reach the required amount of nuclear energy to counteract the contraction post He-b. This means that the beginning of C-burning is in fact happening earlier after the end of He-burning. This leads to a C-burning lifetime longer than the ones obtained with the CF88 rates. This behaviour is consistent with that seen in Fig. 4, where lower reaction rates led to reaching larger densities to burn Carbon, and hence a smaller C-b lifetime.

It is a well-known fact that the C-burning phase is the longest phase of the evolution of massive stars when large neutrino emissions occurs (Arnett 1972; Woosley 1986). In Fig. 7, we can see that in the central regions of the 25 $M_\odot$ model at the middle of the C-burning phase, the energy evacuated through neutrino emissions is nearly always superior to that produced by nuclear burning. Thus, in that phase, the evolution of the stellar core is driven mainly by neutrino emissions. The total quantity of entropy lost by the central region during the whole C-burning phase depends on the product of the time-averaged rate of neutrino emission during that phase and its duration. In the Hin model, the duration is shortened but on the other hand the entropy at the end of that phase not only depends on its duration but also on other factors, such as the neutrino emissions and the nuclear energy production rate. In fact, we can see that the Hin model loses more energy through neutrino emission than the CF88 and HinRes models. We can moreover notice in Fig. 4, that the Hin model crosses more rapidly the degeneracy limit than the other models, implying that it has lost more entropy than the other models during the C-burning phase and thus becomes sensitive to degeneracy effects at earlier stages. This may have important consequences for the ultimate fate of the star, the consequence of the core collapse and the nature of the stellar remnant (see the interesting discussion in Woosley 1986, where the link between the dura-
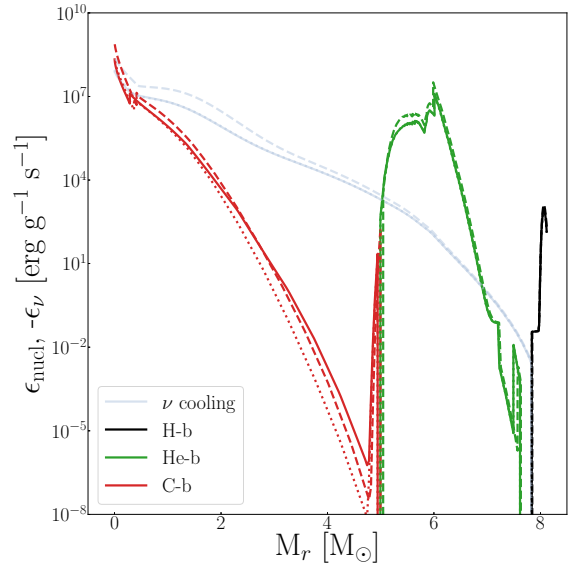
Fig. 7. Energy production at the mid-point of C-burning (when half the central ^{12}C has been consumed since the beginning of C-b) for 25 $M_\odot$ models for different ^{12}C + ^{12}C reaction rates. The CF88, Hin and HinRes models are plotted in plain, dashed, and dotted lines, respectively.

tion of the C-burning phase and these different aspects are discussed). We defer, however, a detailed discussion of this point to a future work where more advanced stages of the evolution will be computed using a new version of GENEC accounting for the radial acceleration term and for a more detailed nuclear reaction network.

5. Impact on detailed nucleosynthesis

In this paragraph, we discuss the impact of the changes of the carbon fusion rates on the detailed composition resulting from C-burning. For this purpose, we used what we call here a 'one-layer model' (Choplin et al. 2016). Instead of computing the evolution of detailed stellar models composed of many hundreds or thousands of layers[1], we compute here the evolution of the abundances in only one layer. This simplification allows the use of a much more extended nuclear reaction network. The nuclear reaction network in the 'one-layer model' follows the evolution of the abundances of 1454 isotopes. The code receives as an input an initial distribution of abundances (i.e. the abundances at the beginning of the core carbon-burning phase) and an evolutionary path in the temperature and density plane representative of the core C-burning phase in a star. These input ingredients are taken from the CF88 25 $M_\odot$ stellar model computed for the present paper. We note that using a 1454 elements network would be very computationally demanding if included in the build-up of stellar models. The stellar models are here computed with a reduced nuclear reaction network that accounts for all the reactions producing significant amounts of energy. Such reduced networks are sufficient to compute reliable stellar structures. On the other hand, this reduced network may miss some reactions that are not important for the energetic but have an impact on the abundances of some elements. This is what we

---

[1] A stellar model computes the evolution as a function of time of the physical quantities at different positions (layers) inside the star. In GENEC, the variables are temperature, pressure, luminosity, radius, and chemical composition, while the independent variable is the mass coordinate.
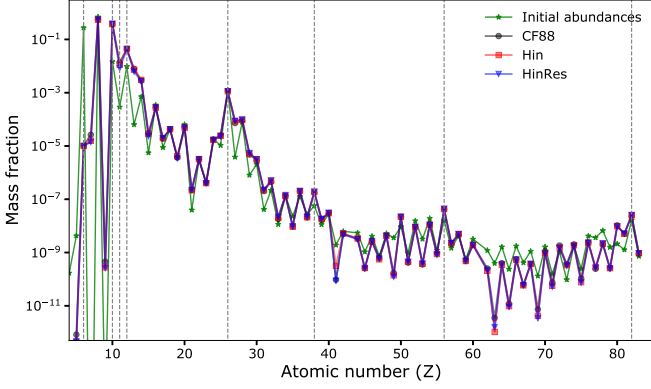
Fig. 8. Comparisons between the abundances before (green) and at the end of the core C-burning phase (black, red and blue) obtained with three different sets of rates for the ^{12}C + ^{12}C reactions. The 8 dashed vertical lines highlight from left to right the carbon ($Z = 6$), neon ($Z = 10$), sodium ($Z = 11$), magnesium ($Z = 12$), iron ($Z = 26$), strontium ($Z = 38$), barium ($Z = 56$), and lead ($Z = 82$).

Fig. 9. Abundances obtained at the end of the C-burning phase normalised to the final abundances obtained using the CF88 rate. Only the elements with a mass fraction greater than 10^{-8} (in either the first or second model) are considered.

want to check here by using a "one-layer model". Three different "one-layer models" are computed. The first one uses the CF88 rates for the reactions ^{12}C(^{12}C,α)^{20}Ne, ^{12}C(^{12}C,p)^{23}Na, and ^{12}C(^{12}C,n)^{23}Mg. The second and third models use rates from Hin model and HinRes model respectively for ^{12}C(^{12}C,α)^{20}Ne and ^{12}C(^{12}C,p)^{23}Na, and we use the recent experimental rates from Bucher et al. (2015) for ^{12}C(^{12}C,n)^{23}Mg.

Figure 8 shows the mass fraction of the elements up to bismuth ($Z = 83$) at the beginning of the C-burning phase (see the green pattern) and at the end of it using CF88, Hin, and HinRes rates (black, red, and blue lines, respectively). The comparison between the red and black,green, and blue lines shows the impact of the C-burning. As expected, we see that the two elements that are produced the most by carbon burning are ^{20}Ne and ^{24}Mg; ^{23}Na is also produced by this phase, but as indicated in the introduction, most of it has been transformed into ^{20}Ne. Interestingly, we can see that strontium ($Z = 38$) is slightly enhanced during the C-burning phase. Strontium is produced by slow neutron capture, the neutrons being released by the reaction ^{13}C(α,n)^{16}O reaction (Pignatari et al. 2013). Barium ($Z = 56$) and lead, also produced by neutron capture, are also slightly enriched.

If we compare the final abundances obtained with the different rates for the ^{12}C + ^{12}C reaction, globally we see that the changes remain very modest and are hardly visible in Fig. 8. Figure 9 represents the abundances normalised to the final abundances obtained using the CF88 rate. Only the elements with a significant mass fraction ($>10^{-8}$) are shown.

Very generally, we see that the final abundances obtained with the Hin rate show less difference with those obtained with the CF88 rate than the abundances obtained with the HinRes rate. The differences between the abundances obtained with the different rates never go beyond a factor of 2. After phosphorus (P), the biggest differences are about 20% (for Co and As).

To give a more detailed account, we first note that, as expected, since we show the situation when the carbon has been burnt, there is (by construction) no differences for the carbon abundances. Other abundant α-nuclei like ^{16}O, ^{20}Ne, ^{24}Mg are modestly affected in this 'one-layer' model. The largest differences arise for nitrogen and sodium. The nitrogen mass fraction is however very small ($\sim 10^{-5}$), while the sodium mass fraction is ~ 0.1. Aluminium and phosphorus also show some differences. These differences are more remarkable for aluminium which has
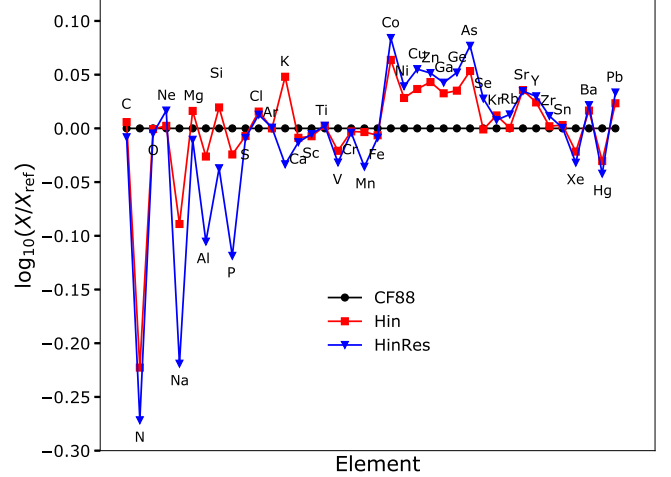
a mass fraction of about 0.01 (the phosphorus mass fraction is only about 10^{-5}). On the whole, these 'one-layer' computations demonstrate that the abundant element that is the most affected by a change of the carbon fusion rate is ^{23}Na. For the high Z elements, the different rates do not especially affect their abundances at the end of the C-burning phase.

The abundance differences obtained in Fig. 9 are too small to have an impact on the evolution and structure of the star during the last evolutionary stages. The nucleosynthesis may nevertheless be impacted: a different Na abundance after the end of core C-burning should impact the production of ^{26}Mg through ^{23}Na(α,p)^{26}Mg (Arnett 1974; Whitmire & Davids 1974). The protons given by this reaction should also increase the production of ^{26}Al through ^{25}Mg(p,γ)^{26}Al (Iliadis et al. 2011).

When we look at the lifetime of such 'one-layer model', we obtain a quite similar C-burning lifetime between the CF88 and the HinRes model (respectively, 0.31 and 0.37 kyr) due to the similar reaction rates in this temperature range. The Hin model lifetime is about eight times longer than the CF88 model. This is due to the absence of the resonance in the Hin model. This lowers the ^{12}C + ^{12}C rate by about 1 dex at 0.8 GK (Fig. 2). Consequently, the carbon takes more time to burn. This is the opposite of what is obtained in stellar models, where the use of the Hin rate produces a shortening of the C-burning lifetime. This comes from the fact that, in the 'one-layer model', there is no possibility for any feedback between the energy produced by the nuclear reactions and the path followed in the temperature and density plane. The path remains the same whatever rate is used. Thus, the model with the lower rate simply takes more time to consume the carbon.

6. Summary and conclusions

In this work, we present new ^{12}C + ^{12}C nuclear reaction rates both in the form of a table and of analytical fits, as well as the uncertainties from the cross section measurements. Experimental data were analyzed with Hin and HinRes response functions, with the latter giving a more accurate approximation. Taking into account the width of the Gamow peak yields a sensitivity of the present experimental data to reaction rates down to temperatures of 0.60 GK, within one-sigma confidence intervals. In this tem-

perature range, the interpolation of the cross sections measured by STELLA is the only input required to determine the reaction rates. This coincides with the effective C-burning temperatures region for both nuclear fusion scenarios investigated (i.e. Hin and HinRes scenarios), for stellar-evolution models of 12 and 25 $M_\odot$ stars studied in this work. We therefore conclude that the direct measurement from Fruet et al. (2020) can provide the experimental input required for stellar evolution models.

Before we review the main impacts of the new rates on the stellar models, we recall here that the evolution of a star is mainly governed by gravity, which tends to contract more and more the central regions. The contraction is stopped during the main nuclear phases because the nuclear reaction allows the pressure gradients to be maintained for long times. During the nuclear burning phases, the nuclear energy released per unit time and mass cannot change much. Indeed, any decrease of it implies a contraction, thus an increase of the temperature (in case of a perfect gas equation of state) and thus an increase of the energy released by nuclear reactions. Vice-versa, an excess of energy produced by nuclear reactions produces an expansion, a cooling and thus a decrease of the nuclear reaction rates. So at order zero, when a nuclear reaction rate important for the production of energy is changed, the energy released remains constant while the temperature changes. Of course, these temperature changes have repercussions on the detailed structure of the star and numerical models are needed to deduce the consequences. We note, however, that because nuclear reaction rates are very sensitive to very small change of the temperature, only a small change of the temperature needs to occur to compensate for a given change of the rate. This line of reasoning allows one to understand why even significant change in a nuclear reaction rate may have only modest effect on the stellar structure.

Although some of the rates differ by more than an order of magnitude at temperatures around 0.8 GK, the models outputs are only slightly changed. We find that in models computed with the lower rate (Hin case), the core C-burning occurs at central temperatures that are higher by about 10%. As a consequence, the carbon burning phase is shortened by about a factor of two. This may impact the ultimate phases before the core collapse and have consequence for the type of event subsequent to that collapse (supernova or not) and for the nature of the stellar remnant (neutron star or black hole). We defer this aspect to a future work, when our stellar evolution code is adapted to the computation of these last stellar evolution phases, a detailed discussion on how these rates will impact the initial condition of the core collapse. Concerning the composition of the supernova ejecta (assuming a neutron star is formed), the use of the lower Hin rate may impact some isotopes such as ^{20}Ne that are found to be enhanced by an order of magnitude in models computed with it.

In addition to the investigations carried out on the impact of the reaction rates determined in this work on the C-burning phase of massive stars, other studies of their impacts could be made on cases where the carbon fusion reaction plays a key role at lower temperatures. This is the area where the discrepancies with older rates is the greatest, such as the C-burning in intermediate-mass stars, type Ia supernovae, or even in superbursts (Strohmayer & Brown 2002).

References

Aguilera, E. F., Rosales, P., Martinez-Quiroz, E., et al. 2006, Phys. Rev. C, 73, 064601
Almqvist, E., Bromley, D. A., & Kuehner, J. A. 1960, Phys. Rev. Lett., 4, 515
Arnett, W. D. 1972, ApJ, 176, 699
Arnett, W. D. 1974, ApJ, 193, 169
Arnett, W. D., & Thielemann, F. K. 1985, ApJ, 295, 589
Arnett, W. D., & Truran, J. W. 1969, ApJ, 157, 339
Back, B. B., Esbensen, H., Jiang, C. L., & Rehm, K. E. 2014, Rev. Mod. Phys., 86, 317
Barrón-Palos, L., Aguilera, E., Aspiazu, J., et al. 2006, Nucl. Phys. A, 779, 318
Becker, H. W., Kettner, K. U., Rolfs, C., & Trautvetter, H. P. 1981, Z. Phys. A At. Nucl., 303, 305
Bucher, B., Tang, X. D., Fang, X., et al. 2015, Phys. Rev. Lett., 114, 251102
Caughlan, G. R., & Fowler, W. A. 1988, At. Data Nucl. Data Tables, 40, 283
Chieffi, A., Roberti, L., Limongi, M., et al. 2021, ApJ, 916, 79
Choplin, A., Maeder, A., Meynet, G., & Chiappini, C. 2016, A&A, 593, A36
Dasgupta, M., Hinde, D. J., Rowley, N., & Stefanini, A. M. 1998, Annu. Rev. Nucl. Part. Sci., 48, 401
Eggenberger, P., Meynet, G., Maeder, A., et al. 2008, Astrophys. Space Sci., 316, 43
Ekström, S., Georgy, C., Eggenberger, P., et al. 2012, A&A, 537, A146
Feldman, G. J., & Cousins, R. D. 1998, Phys. Rev. D, 57, 3873
Fields, C. E., Timmes, F. X., Farmer, R., et al. 2018, ApJS, 234, 19
Fruet, G., Courtin, S., Heine, M., et al. 2020, Phys. Rev. Lett., 124, 192701
Gabriel, M., Noels, A., Montalbán, J., & Miglio, A. 2014, A&A, 569, A63
Gasques, L. R., Brown, E. F., Chieffi, A., et al. 2007, Phys. Rev. C, 76, 035802
Heine, M., Courtin, S., Fruet, G., et al. 2018, Nucl. Instrum. Meth. Phys. Res. Sect. A, 903, 1
High, M., & Čujec, B. 1977, Nucl. Phys. A, 282, 181
Holt, R. J., Filippone, B. W., & Pieper, S. C. 2019, Phys. Rev. C, 99, 055802
Ichikawa, T., Hagino, K., & Iwamoto, A. 2007, Phys. Rev. C, 75, 057603
Illiadis, C. 2015, Nuclear Physics of Stars, 2nd edn. (Weinheim: Wiley-VCH)
Iliadis, C., Champagne, A., Chieffi, A., & Limongi, M. 2011, ApJS, 193, 16
Jacobs, P., & Smilansky, U. 1983, Phys. Rev. B, 127, 313
Jenkins, D., & Courtin, S. 2015, J. Phys. G: Nucl. Part. Phys., 42, 034010
Jiang, C. L., Esbensen, H., Rehm, K. E., et al. 2002, Phys. Rev. Lett., 89, 052701
Jiang, C. L., Rehm, K. E., Back, B. B., & Janssens, R. V. F. 2007, Phys. Rev. C, 75, 015803
Jiang, C., Rehm, K., Fang, X., et al. 2012, Nucl. Instrum. Meth. Phys. Res. Sect. A, 682, 12
Jiang, C. L., Back, B. B., Esbensen, H., et al. 2013, Phys. Rev. Lett., 110, 072701
Jiang, C. L., Santiago-Gonzalez, D., Almaraz-Calderon, S., et al. 2018, Phys. Rev. C, 97, 012801
Kaiser, E. A., Hirschi, R., Arnett, W. D., et al. 2020, MNRAS, 496, 1967
Lamb, S. A., Iben, I., Jr., & Howard, W. M. 1976, ApJ, 207, 209
Li, Y. J., Fang, X., Bucher, B., et al. 2020, Chin. Phys. C, 44, 115001
Maeder, A. 1992, A&A, 264, 105
Mişicu, Ş., & Esbensen, H. 2006, Phys. Rev. Lett., 96, 112701
Patterson, J., Winkler, H., & Zaidins, C. 1969, ApJ, 157, 367
Pignatari, M., Hirschi, R., Wiescher, M., et al. 2013, ApJ, 762, 31
Roberts, O. J., Bruce, A. M., Regan, P. H., et al. 2014, Nucl. Instrum. Meth. Phys. Res. Sect. A, 748, 91
Rolfs, C., & Rodney, W. 1988, Cauldrons in the Cosmos (Chicago: University of Chicago Press)
Simenel, C., Umar, A. S., Godbey, K., Dasgupta, M., & Hinde, D. J. 2017, Phys. Rev. C, 95, 031601
Sparks, W. M., & Endal, A. S. 1980, ApJ, 237, 130
Spillane, T., Raiola, F., Rolfs, C., et al. 2007, Phys. Rev. Lett., 98, 122501
Strohmayer, T. E., & Brown, E. F. 2002, ApJ, 566, 1045
Sukhbold, T., & Adams, S. 2020, MNRAS, 492, 2578
Tan, W. P., Boeltzig, A., Dulal, C., et al. 2020, Phys. Rev. Lett., 124, 192702
Thielemann, F. K., Arnould, M., & Truran, J. W. 1986, in Advances in Nuclear Astrophysics, eds. E. Vangioni-Flam, J. Audouze, M. Casse, J. P. Chieze, & J. Tran Thanh Van, 525
Villante, F. L., & Serenelli, A. 2021, Front. Astron. Space Sci., 7, 112
Weaver, T. A., Zimmerman, G. B., & Woosley, S. E. 1978, ApJ, 225, 1021
Whitmire, D. P., & Davids, C. N. 1974, Phys. Rev. C, 9, 996
Woosley, S. E. 1986, in Saas-Fee Advanced Course 16: Nucleosynthesis and Chemical Evolution, eds. J. Audouze, C. Chiosi, & S. E. Woosley, 1

Appendix A: Tables and analytic formulae

Table A.1 summarizes values of reaction rates for different temperatures. Recommended rates are based on a classical determination of the reaction rates using cross section extrapolation, and lower and upper rates represent the lower and upper limits of recommended rates, using their 1σ uncertainties. The latter comes from experimental uncertainties on cross sections measured by STELLA experiment (Fruet et al. 2020).

Reaction rates have been fitted with the formula from Thielemann et al. (1986), used in the REACLIB library:

$$N_A\langle\sigma v\rangle = \sum_i \exp(a_{i0} + a_{i1}/T_9 + a_{i2}/T_9^{1/3} + a_{i3}T_9^{1/3}$$
$$+ a_{i4}T_9 + a_{i5}T_9^{5/3} + a_{i6}ln(T_9)), \qquad (A.1)$$

where a_i are fitting parameters and T_9 is the temperature in GK. In the case of the Hin model, the best fit was obtained with $i = 1$, and for HinRes model with $i = 2$. The different parameters are reported in Tables A.2 and A.3 for the Hin model and the HinRes model, respectively.

Table A.1. Reaction rates for the ^{12}C + ^{12}C fusion reaction according to different models. Reaction rates are in cm^3 s^{-1} mol^{-1} and temperatures in GK.

T	Hin model			HinRes model		
	Recomm.	Lower	Upper	Recomm.	Lower	Upper
0.11	1.79E-54	1.15E-54	2.42E-54	2.94E-54	1.87E-54	4.00E-54
0.12	4.40E-52	2.89E-52	5.90E-52	7.02E-52	4.58E-52	9.46E-52
0.13	6.03E-50	4.05E-50	8.02E-50	9.39E-50	6.26E-50	1.25E-49
0.14	5.10E-48	3.48E-48	6.71E-48	7.75E-48	5.26E-48	1.02E-47
0.15	2.87E-46	1.99E-46	3.74E-46	4.27E-46	2.94E-46	5.60E-46
0.16	1.14E-44	8.03E-45	1.48E-44	1.67E-44	1.17E-44	2.17E-44
0.18	7.68E-42	5.54E-42	9.82E-42	1.08E-41	7.78E-42	1.39E-41
0.2	2.08E-39	1.53E-39	2.63E-39	2.86E-39	2.10E-39	3.62E-39
0.25	1.53E-34	1.17E-34	1.89E-34	1.98E-34	1.51E-34	2.45E-34
0.3	7.67E-31	6.05E-31	9.29E-31	9.54E-31	7.50E-31	1.16E-30
0.35	6.77E-28	5.45E-28	8.08E-28	8.16E-28	6.56E-28	9.77E-28
0.4	1.79E-25	1.47E-25	2.11E-25	2.16E-25	1.76E-25	2.57E-25
0.45	1.97E-23	1.64E-23	2.30E-23	2.77E-23	2.20E-23	3.34E-23
0.5	1.11E-21	9.37E-22	1.29E-21	2.34E-21	1.75E-21	2.92E-21
0.55	3.75E-20	3.18E-20	4.31E-20	1.27E-19	9.08E-20	1.63E-19
0.6	8.34E-19	7.15E-19	9.54E-19	4.13E-18	2.88E-18	5.38E-18
0.65	1.32E-17	1.14E-17	1.51E-17	8.30E-17	5.75E-17	1.09E-16
0.7	1.59E-16	1.38E-16	1.80E-16	1.11E-15	7.67E-16	1.45E-15
0.75	1.51E-15	1.32E-15	1.70E-15	1.06E-14	7.35E-15	1.39E-14
0.8	1.18E-14	1.03E-14	1.32E-14	7.70E-14	5.36E-14	1.00E-13
0.85	7.73E-14	6.81E-14	8.64E-14	4.46E-13	3.14E-13	5.79E-13
0.9	4.37E-13	3.87E-13	4.87E-13	2.15E-12	1.53E-12	2.77E-12
0.95	2.17E-12	1.93E-12	2.41E-12	8.93E-12	6.44E-12	1.14E-11
1	9.62E-12	8.57E-12	1.07E-11	3.28E-11	2.41E-11	4.15E-11
1.05	3.85E-11	3.44E-11	4.27E-11	1.09E-10	8.15E-11	1.36E-10
1.1	1.41E-10	1.26E-10	1.56E-10	3.34E-10	2.55E-10	4.12E-10
1.15	4.77E-10	4.27E-10	5.26E-10	9.58E-10	7.51E-10	1.16E-09
1.2	1.50E-09	1.34E-09	1.65E-09	2.61E-09	2.10E-09	3.13E-09
1.25	4.40E-09	3.96E-09	4.84E-09	6.81E-09	5.59E-09	8.03E-09
1.3	1.22E-08	1.10E-08	1.34E-08	1.71E-08	1.43E-08	1.99E-08
1.35	3.20E-08	2.88E-08	3.51E-08	4.14E-08	3.53E-08	4.76E-08
1.4	7.99E-08	7.21E-08	8.76E-08	9.72E-08	8.39E-08	1.11E-07
1.45	1.90E-07	1.72E-07	2.09E-07	2.21E-07	1.93E-07	2.49E-07
1.5	4.36E-07	3.94E-07	4.77E-07	4.87E-07	4.29E-07	5.45E-07
1.75	1.61E-05	1.46E-05	1.76E-05	1.65E-05	1.49E-05	1.82E-05
2	3.01E-04	2.72E-04	3.29E-04	3.02E-04	2.73E-04	3.31E-04
2.5	2.70E-02	2.44E-02	2.96E-02	2.70E-02	2.43E-02	2.96E-02
3	7.45E-01	6.69E-01	8.22E-01	7.48E-01	6.71E-01	8.25E-01
3.5	9.69E+00	8.63E+00	1.08E+01	9.79E+00	8.71E+00	1.09E+01
4	7.52E+01	6.65E+01	8.39E+01	7.65E+01	6.75E+01	8.54E+01
5	1.63E+03	1.42E+03	1.84E+03	1.68E+03	1.46E+03	1.90E+03
6	1.47E+04	1.26E+04	1.68E+04	1.54E+04	1.32E+04	1.77E+04

Table A.2. Parameters for recommended, lower and upper reaction rates in the case of Hin model.

a_{ij}	Recomm.	Lower	Upper
a_{10}	7.72E+01	7.77E+01	7.68E+01
a_{11}	6.18E-02	6.39E-02	4.41E-02
a_{12}	-9.45E+01	-9.50E+01	-9.40E+01
a_{13}	-7.73E+00	-7.83E+00	-7.64E+00
a_{14}	-4.35E-01	-4.57E-01	-4.16E-01
a_{15}	3.11E-02	3.33E-02	2.88E-02
a_{16}	2.28E-01	1.64E-01	2.88E-01

Table A.3. Parameters for recommended, lower and upper reaction rates in the case of HinRes model.

a_{ij}	Recomm.	Lower	Upper
a_{10}	7.63E+01	7.68E+01	7.58E+01
a_{11}	4.97E-02	5.12E-02	3.18E-02
a_{12}	-9.37E+01	-9.42E+01	-9.32E+01
a_{13}	-7.60E+00	-7.70E+00	-7.51E+00
a_{14}	-4.19E-01	-4.44E-01	-3.97E-01
a_{15}	2.97E-02	3.21E-02	2.72E-02
a_{16}	3.53E-01	2.95E-01	4.10E-01
a_{20}	3.42E-01	5.07E-01	-3.62E+00
a_{21}	-2.48E+01	-2.48E+01	-2.52E+01
a_{22}	3.25E-01	3.97E-01	3.94E+00
a_{23}	-3.65E-01	-3.32E-01	5.97E-02
a_{24}	1.64E-02	-7.59E-03	-1.45E-01
a_{25}	-7.65E-04	1.68E-03	1.23E-02
a_{26}	-1.29E+00	-1.24E+00	-4.16E-01